Analytical Methods

ROYAL SOCIETY OF CHEMISTRY

PAPER

View Article Online
View Journal

Cite this: DOI: 10.1039/d6ay00371k

A new strategy for improving the precision and accuracy of isotope ratio analysis by quadrupole ICP-MS with the optimization of ion beam trajectory

Xing Li,[a] Haitao Li,[b] Dingwen Zhang,[a] Xin Yang,[a] Yu Cui,[a] Wei Guo,[a] Lanlan Jin[a] and Shenghong Hu *[a]

Non-traditional stable isotopes are widely utilized in geoscience and other fields. However, it remains challenging to analyze many samples quickly with high accuracy and precision. In this study, new optimization strategies are proposed to improve the precision and accuracy of isotope ratio analysis using inductively coupled plasma quadrupole mass spectrometry (ICP-QMS). The instrument voltage parameters of cell entrance/exit voltage (CEV), cell rod offset (CRO), and quadrupole rod offset (QRO) were optimized to control the ion trajectory and reduce mass discrimination. The detector's signal acquisition parameters were also optimized to improve the precision of isotope ratio analysis. After optimization, the mass deviations in B, Sr, and Pb isotope measurements were significantly reduced to −0.25%, −0.13%, and −0.34%, respectively. The proposed isotope analysis method was applied to geological standard reference materials, including AGV-2, BCR-2, BHVO-2, GSR-7, GSD-21, GSD-23, and GSS-14. The measured values of B, Sr, and Pb isotopes were in agreement with the reported values. The precision values (2SD) for B, Sr, and Pb were better than 1.20‰, 0.34‰, and 0.00308, respectively. This approach enables direct analysis of various geological matrices without chemical separation and purification, making it possible to rapidly process large sample batches. It provides a more economical and simpler alternative, favoring the development of isotope-related applications in more fields.

Received 2nd March 2026
Accepted 26th April 2026

DOI: 10.1039/d6ay00371k

rsc.li/methods

1. Introduction

With advances in thermal ionization mass spectrometry (TIMS) and multi-collector inductively coupled plasma mass spectrometry (MC-ICP-MS), analysis of non-traditional stable isotopes has advanced research in geoscience, cosmochemistry, archaeology, clinical medicine, and environmental science. However, TIMS and MC-ICP-MS have drawbacks, including the complexity and time-consuming nature of separation and purification, as well as the high cost of experimental procedures. It is difficult to analyze a large number of samples. Inductively coupled plasma quadrupole mass spectrometry (ICP-QMS) is a user-friendly approach that offers high sample throughput, good tolerance to matrix complexity, straightforward sample preparation, and the capability for isotope analysis. Particularly in environmental and agricultural science research, ICP-QMS demonstrates significant advantages for tracing sources of heavy metal pollution and identifying the origin of agricultural products through isotope analysis of large numbers of samples. Improving the precision and accuracy of ICP-QMS isotope analysis is always a challenge.

Many reports have focused on isotope analysis using ICP-QMS. These advances involve two main strategies: (1) methodological optimization, including internal and external standardization, matrix matching, and signal processing, and (2) instrumental parameter optimization involving the signal detector and operating conditions.

For methodological optimization, Santos *et al.*[1] used external standardization and matrix-matching to mitigate space-charge and mass discrimination effects in U-rich matrices. Prolonging the acquisition time for low-abundance isotopes ensured precision comparable to that for high-abundance isotopes, yielding RSDs of 0.1–0.3% across varying U concentrations. A concentration-gradient method for isotope analysis with ICP-QMS was developed by Dronov *et al.*[2] The slope of the concentration gradient represented the isotope ratio, and the intercept represented the solvent blank and interference, which completely avoided the influence of isobaric interference on isotope determination. The precision of the isotope analysis was 0.62‰. Using dynamic reaction cell technology to analyze

[a]State Key Laboratory of Geomicrobiology and Environmental Changes, School of Earth and Planetary Sciences, China University of Geosciences, Wuhan 430074, China. E-mail: shhu@cug.edu.cn

[b]Jiangxi Provincial Key Laboratory of Environmental Pollution Prevention and Control in Mining and Metallurgy, School of Resource and Environmental Engineering, Jiangxi University of Science and Technology, Ganzhou 341000, China

the $^{44}Ca/^{40}Ca$ isotope ratio in a 60 ng g^{-1} calcium solution, Boulyga *et al.*[3] achieved an accuracy of 0.03–0.05% within a single 6 minute analysis cycle. This method has potential use for geological, archaeometric, and biological applications as well as in authentication studies of goods and artifacts. Misra *et al.*[4] proposed calculating Li isotope ratios from raw mass-scan data (not instrument-averaged ratios) and processing them offline in Excel. Combined with cold plasma and soft extraction, this approach achieved high precision (<±0.8‰, 2σ), low blanks (1.0 ± 0.5 pg), and minimal mass consumption (<0.2 ng, five replicate analyses). Similarly, Liu *et al.*[5] used a sample-standard bracketing method to analyze Li isotopes with ICP-QMS and obtained a 2SD value of 1.1‰. The analytical results demonstrated that ICP-QMS could achieve long-term precision and accuracy comparable to TIMS and MC-ICP-MS for Li isotope analysis.

For instrumental parameter optimization, Ulrich *et al.*[6] reported significant repeatability errors during multi-mass Pb isotope analysis (NIST SRM 982), highlighting the need to minimize the number of mass numbers in quadrupole-based isotopic analyses and to avoid precision degradation caused by peak hopping. Marguí *et al.*[7] optimized the scan conditions and dead time for Pb isotopes, achieving 0.01–0.2% standard deviation during NIST SRM 981 and successfully tracing Pb pollution sources. Salazar *et al.*[8] reported Pb isotope precision (0.06–1.3% RSD) using identical ICP-QMS instruments in two laboratories, with a large fluctuating range presumably due to limited repetitions. This method demonstrated good accuracy and precision in soil and geologic samples, with minimal matrix-dependent effects. Usman *et al.*[9] found Pb isotope precision (within-sample: 0.08–0.16% RSD; between-sample: 0.31–2.58% RSD) independent of dwell time, whereas Godoy *et al.*[10] improved Pu and U isotope precision to meet IAEA requirements by optimizing dwell times under fixed analysis durations. Zheng *et al.*[11] further showed that excessively short dwell times (<0.1 ms) distorted mass spectra, while longer dwell times enhanced the low-abundance isotope counts, achieving <0.5% RSDs for $^{235/238}U$ and <2.0% RSDs for $^{234/238}U$ in sediment samples. Mathuthu *et al.*[12] used a dual-mode detector and a collision cell interface to achieve excellent sensitivity and precision (<0.2% RSD for $^{107/109}Ag$), enabling Pb source identification in ore samples. Our group[13] demonstrated the superiority of pulse mode (<0.1% RSD) over analog/dual modes, highlighting its importance for high-precision ratio measurements. Grotti *et al.*[14] enhanced sensitivity by optimizing instrument voltages (*e.g.*, QRO), enabling the determination of ^{204}Pb-based isotopic ratios at a part-per-billion level by quadrupole ICP-MS. The internal precision was ~0.4% at 1 mg L^{-1} and ~0.2% at 10 mg L^{-1}, the external precision was better than 0.34% (% RSD, $n = 35$), and differences from the reference values were lower than 2‰. A recent review by Penanes[15] confirmed ICP-MS's maturity for isotope analysis, with technological advances enabling the detection of previously undetectable natural variations. While signal acquisition optimization approaches in ICP-QMS have significantly enhanced precision, isotopic accuracy still largely relies on mathematical corrections, which can be problematic for large deviations. To solve this fundamental challenge, advancing ion beam trajectory optimization is a critical pathway to achieving intrinsically accurate isotope ratios. Sakata *et al.*[16] simulated ion trajectories at the ICP-MS plasma interface, providing key insights into beam behavior. Moreover, Kivel *et al.*[17] stated, from a theoretical point of view, that the trajectories of ions in an electric field are governed by the interaction between the mass-to-charge ratio and the kinetic energy.

In this study, we used PerkinElmer NexION™ 350D ICP-QMS to achieve good accuracy and precision in isotope analysis. The instrument voltage parameters, including cell entrance/exit voltage (CEV), cell rod offset (CRO), and quadrupole rod offset (QRO), were optimized to control the ion trajectory and reduce mass discrimination. The detector's signal acquisition parameters were optimized to improve the precision of isotope ratio analysis. The results of geological standard analyses were in good agreement with the reported values. This method is suitable for the direct analysis of large numbers of samples without purification, demonstrating reliability and potential for broader application.

2. Experimental

2.1 Instrumentation

PerkinElmer NexION™ 350D ICP-QMS was used in this work. The operating parameters were optimized with a tuning solution (1 ng mL^{-1} Be, Mg, In, Ce, Pb, and U) prior to determination to obtain the maximum signal intensities and the minimum oxide formation rate and doubly charged ratio. The isotope standard reference solutions for NIST SRM 951a (B), NIST 987 (Sr), and NIST 981 (Pb) at 100 μg L^{-1} were used to optimize the CEV, CRO, and QRO voltages, ensuring the ratios of measured isotope values to the recommended values were close to 1. Typical instrumental operating conditions and parameters are listed in Table 1.

2.2 Reagents and materials

Guaranteed-grade nitric acid (HNO_3) and hydrofluoric acid (HF) were purchased from Sinopharm Chemical Reagent Ltd (China). Both acids were distilled twice using a homemade PTFE sub-boiling system. Ultrapure water (18.2 MΩ cm) was produced by a Millipore system (USA).

Isotope standard reference materials, including NIST SRM 951a, NIST SRM 987, and NIST SRM 981, were obtained from

Table 1 The ICP-QMS instrument operational settings

ICP-QMS instrument	PerkinElmer 350D
RF power	1500 W
Nebulizer gas flow	0.9 L min^{-1}
Auxiliary gas flow	1 L min^{-1}
Plasma gas flow	16 L min^{-1}
Dead time	35 ns
Detector mode	Pulse
Pulse stage voltage	1050 V
Analog stage voltage	−1900 V

the National Institute of Standards and Technology (NIST, USA). These reference materials were dissolved with 2% HNO_3 and serially diluted to appropriate concentrations for subsequent analysis.

Geological standard reference materials (AGV-2, BCR-2, BHVO-2) were procured from the United States Geological Survey (USGS, USA). The certified reference materials GBW07109 (GSR-7), GBW07364 (GSD-21), GBW07366 (GSD-23), and GBW07428 (GSS-14) were obtained from the Institute of Geophysical and Geochemical Prospecting (P.R. China).

2.3 Sample digestion

For routine element and isotope analysis, approximately 50 mg of each sample (rock, sediment, and soil) was weighed into high-pressure bombs. Then 1 mL of concentrated HNO_3 and 1 mL of concentrated HF were added to each bomb. The bombs were sealed and heated to 190 °C in an electric oven for 48 h. After cooling to room temperature, the samples were removed from the oven and dried on a heating plate at 115 °C. Then they were dissolved in 1 mL of concentrated HNO_3 and evaporated to dryness, and the procedure was repeated twice to remove excess HF. Afterward, 3 mL of 30% (v/v) HNO_3 was added to the samples, followed by resealing and heating in an oven at 190 °C for 12 h to re-dissolve the resultant salt. Finally, the solution was transferred to a PE bottle and diluted with 2% HNO_3 to 50 g for the determination of Sr and Pb by ICP-QMS.

For B isotope analysis, approximately 100 mg of each sample was weighed into a pre-cleaned 10 mL PFA cup. We added 100 μL of 1% mannitol, 100 μL of H_2O_2, and 1 mL of HF. The beaker was tightly capped and placed on a hot plate at 60 °C for 3 days. Then, 2 mL of ultrapure water was added to the PFA cup. The solution and sediment were transferred to a pre-cleaned polypropylene (PP) tube and centrifuged. The supernatant was collected, and 2 mL of ultrapure water was added to the tube to wash the sediment. After further centrifugation, the supernatant was collected and transferred into a pre-cleaned 15 mL PFA beaker. We added 100 μL of 1% mannitol to the beaker to minimize boron volatilization losses during drying. Then, the 15 mL PFA beaker was placed on a hot plate set to 55 ± 2 °C. Drying typically took 2–3 days. The dried samples were redissolved in 2 mL of ultrapure water. The solution was further transferred to a PE bottle and diluted with 2% HNO_3 to 50 g for determination by ICP-QMS.

2.4 Isotope analysis

After sufficient plasma warm-up and routine tuning to achieve optimal conditions, samples were introduced by self-aspiration to minimize air-bubble entrainment and to avoid peristaltic pump pulsation effects. The analytical method was switched to isotope ratio mode with pulse-only counting detection. Each analysis measured only one isotope ratio. The lens voltage was fixed to stabilize ion beam trajectories and re-optimized for the maximum target isotope signal intensity. Isotope standard solutions were diluted to match sample concentrations. Isotope ratios were measured using the standard-sample bracketing method. The reference materials were NIST SRM 951a for B, NIST SRM 987 for Sr, and NIST SRM 981 for Pb. Results were expressed as delta values for B and Sr and as isotope ratios for Pb, according to analytical conventions.

3. Results and discussion

3.1 Effect of voltage parameters on isotope ratio accuracy

Instrument voltage parameters enable the control of ion beam trajectories to mitigate mass discrimination, thereby improving the precision and accuracy of isotope ratios. Fig. 1 shows the ion trajectory diagram of PerkinElmer NexION™ 350D ICP-QMS. Ions generated in the plasma source passed through a triple cone interface. Then ions underwent 90° deflection through an electrical lens for mass-to-charge (m/z) preselection and were subsequently focused in the universal cell for energy stabilization. Finally, ions were filtered by the quadrupole and detected

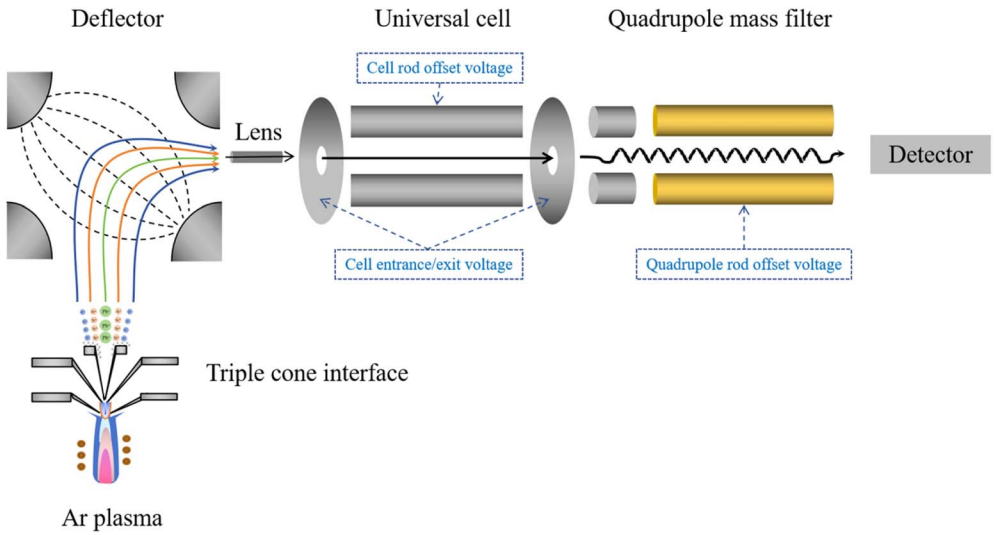

Fig. 1 The ion trajectory diagram for the instrument.

by the detector. Three critical voltage parameters control trajectory modulation: (1) cell entrance/exit voltage (CEV), which is applied to both sides of the universal cell, (2) cell rod offset (CRO), which adjusts the deflection of the cell quadrupole, and (3) quadrupole rod offset (QRO), which regulates the deflection of the mass filter. In order to investigate the effects of these three critical voltage parameters on isotope analysis over the full mass range, we evaluated the signal sensitivity, isotope ratio accuracy, and precision (RSD) using 100 μg L^{-1} solutions of NIST SRM 951a (B), NIST 987 (Sr), and NIST 981 (Pb).

3.1.1 Cell entrance/exit voltage. The cell entrance/exit voltage (CEV) regulates ion kinetic energy during universal cell transit, maintaining the same value at each side of the cell. Its purpose is to stabilize ion kinetic energy across cell boundaries. The entrance voltage determines the initial energy levels, which can lead to a kinetic energy deficit or an overflow for ions of different masses. The exit voltage controls the kinetic energy of the ions leaving the universal cell and directly influences the transmission efficiency through the subsequent quadrupole mass filter. This dual effect can be considered in combination, leading to a positive bias in the light/heavy ratio if the signal enhancement of lighter isotopes dominates, and a negative bias if scattering losses dominate. Inappropriate CEV settings may lead to signal losses and isotope ratios that deviate from their true values.

To investigate the effects of CEV on isotope analysis, experiments were performed over a CEV range from +2 V to −20 V (at 1 V intervals) until signal attenuation. Variations in signal intensities, isotope ratios, and the precision values of B, Sr, and Pb isotopes under different voltage conditions are shown in Fig. 2. The signal sensitivity curves for B, Sr, and Pb exhibited distinct peaks and plateau regions at specific voltage values. The peak sensitivity of the lighter-mass elements occurred at more negative voltages. The peak sensitivity of B occurred at −15 V and −9 V, respectively, and there was a plateau between −18 V and −2 V. Beyond this range, sensitivity decreased sharply due to insufficient kinetic energy or ion beam defocusing. Similarly, the peak sensitivity of Sr was at −7 V, and the plateau was between −16 V and −4 V, while the plateau of Pb was between −8 V and 0 V. The variations of isotope ratios indicated that all three isotope ratios were closer to their true values at specific voltage values (−11 V, −4 V, and 0 V for B; −17 V, −12 V, and −11 V for Sr; and −5 V, −1 V, and 0 V for Pb), and the range of variation was smaller near 0 V. As the CEV became more negative, the oscillations of the ratios became amplified and the ranges of variations became larger. This was due to the combined effect of reduced collisional losses and enhanced ion beam defocusing, leading to repeated deviations of the measured value from the true value and larger fluctuations as the kinetic energy increased. The variations of the precision of the isotope ratio were not obvious, and the precision values could be less than 1‰ under optimal conditions. Notably, the poorer precision of the B isotope at 1 V was due to insufficient sensitivity. Moreover, maximum signal strength did not guarantee the most accurate isotope ratio. The CEV voltage values for B, Sr, and Pb isotopes were finally set to −11 V, −11 V, and −2 V, respectively.

3.1.2 Cell rod offset voltage. The cell rod offset voltage (CRO) is a bias voltage applied to the quadrupole in the universal cell, controlling ion beam focusing and transport.

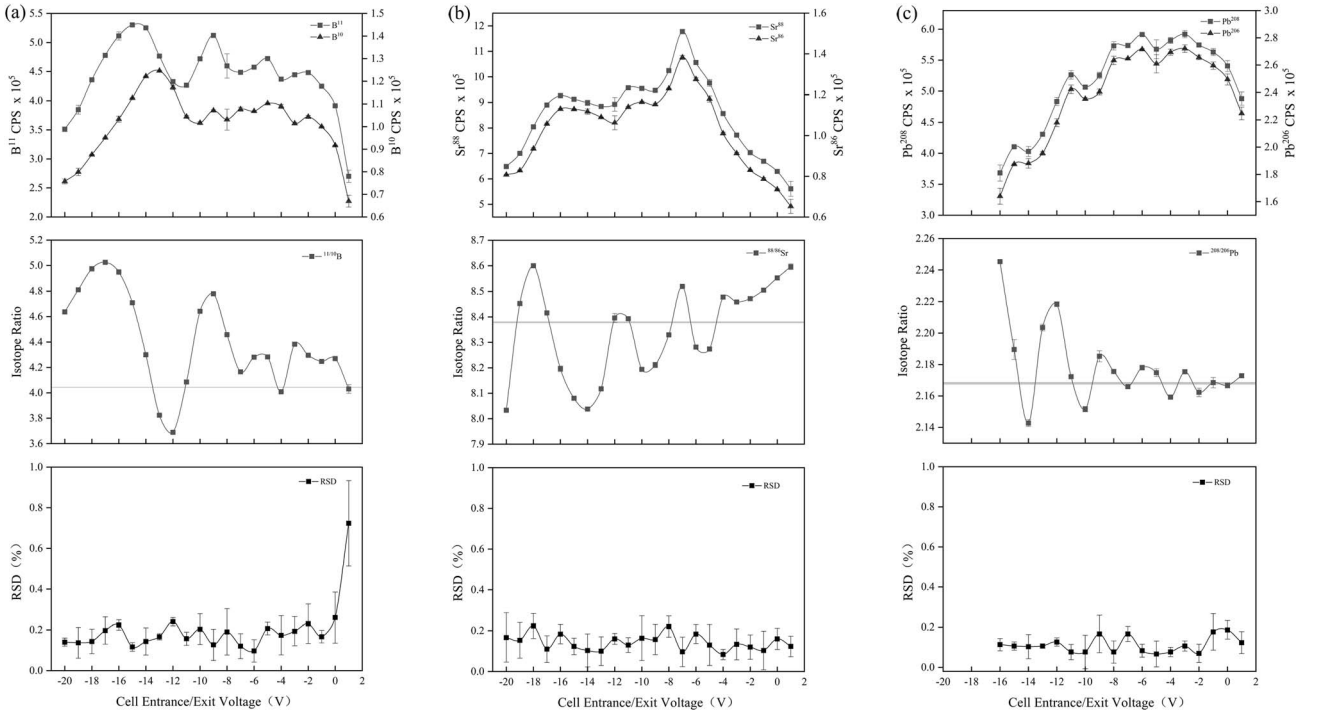

Fig. 2 The signal intensities, isotope ratios, and precision values of B, Sr, and Pb isotopes under different CEV conditions: (a) B, (b) Sr, (c) Pb. The gray-shaded area indicates the recommended value of the isotope ratio.

Making CRO more negative focuses the ion beam more tightly and brings the ion trajectory closer to the quadrupole's central axis, reducing collision and scattering losses. However, excessive negative voltages amplify space charge effects, leading to ion repulsion. These two effects should be considered together based on the actual situation.

To investigate the effects of CRO on isotope analysis, experiments were performed over a range of CRO values from +1 V to −16 V until signal attenuation. Variations in signal intensities, isotope ratios, and the precision values of B, Sr, and Pb isotopes under different voltage conditions are shown in Fig. 3. Sensitivity profiles showed multiple peaks for the three elements, with no clear pattern as the signals fluctuated. This reflected competing interactions between beam focusing and space charge effects. Peaks emerged when focusing was dominant, whereas valleys corresponded to signal attenuation caused by space charge. The variations of the isotope ratios of B, Sr, and Pb showed that the measured values fluctuated repeatedly around the recommended values. When CRO was more negative, lighter isotopes were more susceptible to electric field focusing, thereby significantly improving their transmission efficiency. Heavier isotopes had a smaller increase in transmission efficiency due to their higher kinetic energy and more stable trajectories, which could cause a positive bias in the light/heavy ratio. Conversely, when CRO was more positive, the ion beam diffused, and the lighter isotopes were more likely to deviate from their trajectories due to their relatively lower kinetic energy, leading to a negative bias. The precision values of the three isotopes could be less than 1‰ under optimal conditions and were not significantly correlated with CRO variations. The CRO voltage values for B, Sr, and Pb isotopes were set to −9 V, −6 V, and −6 V, respectively.

3.1.3 Quadrupole rod offset voltage. The quadrupole rod offset (QRO) voltage is a bias voltage applied to the main quadrupole mass filter. The Mathieu equation is the mathematical formula governing the trajectory of ions within a quadrupole. Ion trajectory stability is determined by the parameters a and q, *i.e.*, the DC-to-RF voltage (U/V) ratio. The solutions to the Mathieu equation represent multiple stable regions. Usually, only the first stable region is considered, as it has the widest range, higher ion transport efficiency and greater stability. Within the first stable region, the sensitivity follows a normal distribution, whereas the isotope ratios exhibit distinct patterns. Specifically, QRO affects the U/V ratio, which determines the position of the stable region, leading to the preferential transport of ions with specific m/z values. Making QRO more negative shifts the stable region toward higher m/z values, preferentially transmitting heavier isotopes while excluding lighter ones, leading to a negative bias in light/heavy ratios. Conversely, making QRO less negative lowers the m/z threshold, potentially filtering heavier isotopes and generating a positive ratio bias. During wide-range QRO variations, the stability of ion trajectories with different m/z values may undergo periodic oscillations, leading to periodic fluctuations in isotope ratios. This phenomenon occurs when variations in voltage parameters align with the RF periodic dynamics of the Mathieu equation under specific conditions. Incorrect QRO settings introduce systematic deviations in ion transport efficiency across different m/z values, leading to isotope ratios that deviate from true values.

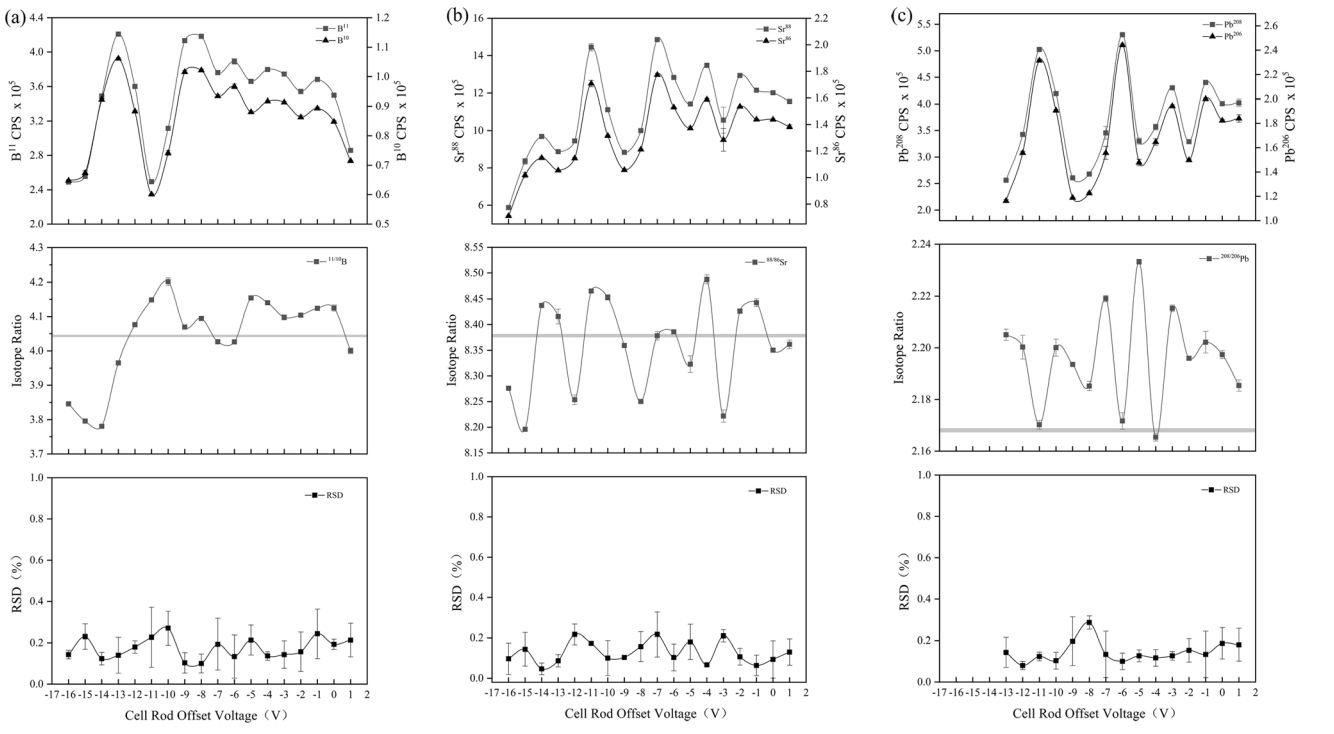

Fig. 3 The signal intensities, isotope ratios, and precision values of B, Sr, and Pb isotopes under different CRO conditions: (a) B, (b) Sr, (c) Pb. The gray-shaded area indicates the recommended value of the isotope ratio.

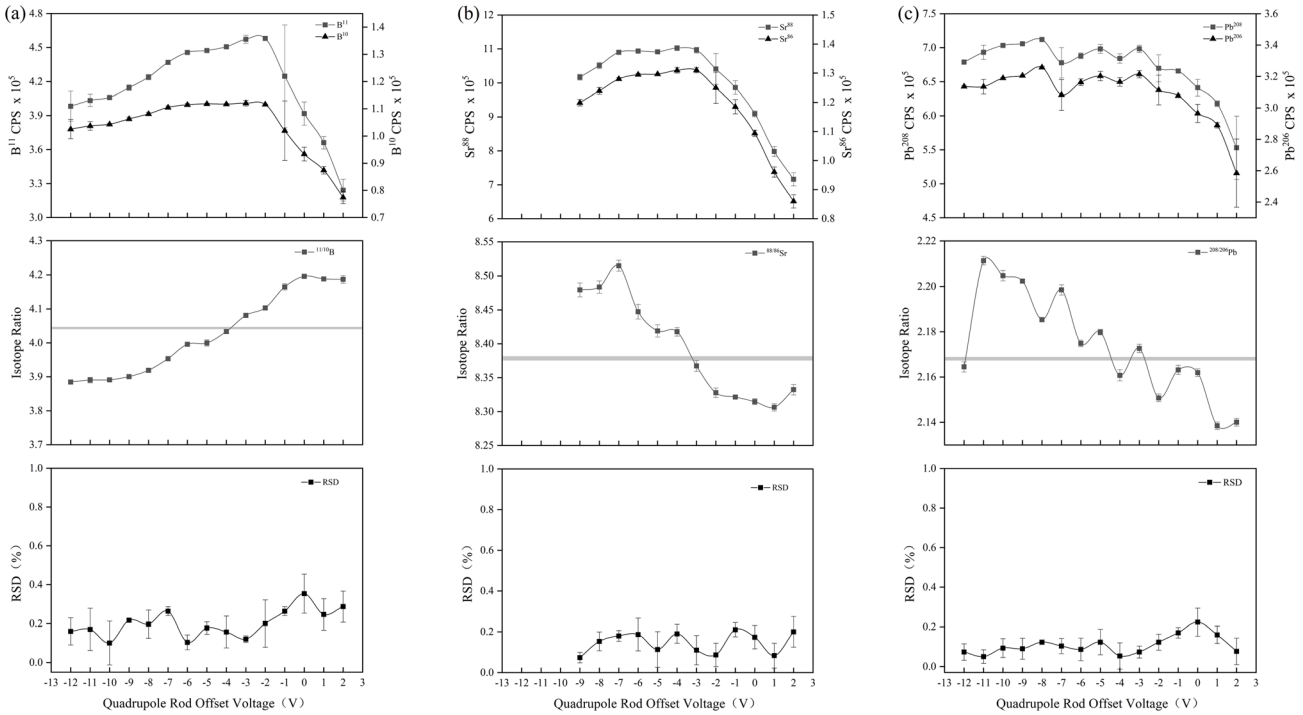

Fig. 4 The signal intensities, isotope ratios, and precision values of B, Sr, and Pb isotopes under different QRO conditions: (a) B, (b) Sr, (c) Pb. The gray-shaded area indicates the recommended value of the isotope ratio.

To investigate the effects of QRO on isotope analysis, experiments were performed across a QRO range from +2 V to −12 V until signal attenuation. Variations in signal intensities, isotope ratios, and the precision values of B, Sr, and Pb isotopes under different voltage conditions are shown in Fig. 4. The sensitivities of B, Sr, and Pb changed little when the QRO voltage was set to negative values. However, when the QRO voltage was set to a positive value, element sensitivity decreased significantly. The Sr and Pb isotopic ratios decreased systematically as the QRO voltage became more positive, while the B isotopic ratio increased. The precision of B and Sr isotopes could be controlled within 1‰ under optimal conditions, and the precision of Pb isotopes was within 1‰ in most cases. The QRO voltage values for B, Sr, and Pb isotopes were set to −4 V, −3 V, and −4 V, respectively.

3.1.4 Mass bias. In conventional optimization, the parameter values that yield the highest signal sensitivity are typically considered optimal. As shown in Fig. 2–4, for B isotopes, the signal was optimal when CEV was −15 V, with a mass deviation of 16.4% in the isotope ratio at that point. CRO yielded the highest signal at −13 V, with a ratio deviation of 1.95%. QRO produced the strongest signal at −15 V with a deviation of 1.47%. The combined effect of these three voltages ultimately resulted in a mass deviation of 15.8% for the B isotope ratio. For the Sr isotope, the ratio deviation was 1.68% when the CEV signal was highest, −0.004% when the CRO signal was highest, and 0.47% when the QRO signal was highest, with a combined effect of 2.15%. For the Pb isotope, the ratio deviation was 0.34% when the CEV signal was highest, 0.17% when the CRO signal was highest, and 0.80% when the QRO signal was highest, with a combined effect of 1.30%.

After optimizing the voltage parameters, the mass deviations in B, Sr, and Pb isotope measurements were significantly reduced to −0.25%, −0.13%, and −0.34%, respectively. Since the ion beam trajectory is influenced by multiple factors, optimizing the voltage parameters reduced the interference from these combined factors or made the interference situation more consistent. This ensured that ion transmission losses or transmission efficiencies across different mass numbers remained stable or comparable, rather than exhibiting random fluctuations. Consequently, isotope ratios approached true values more closely, with no significant loss in signal intensity, and measurement precision remained reliable.

3.2 Effect of detector signal acquisition parameters on isotope precision

The effects of detector parameters, including the number of scans/readings/replicates and dwell time, on isotopic precision were investigated using 100 μg L^{-1} standard solutions (NIST SRM 951a, NIST SRM 987, and NIST SRM 981). Fig. 5(a) shows the effects of the number of scans on isotope precision. The optimal precision gradually approached the theoretical limit of ≤1‰ RSD after 600 scans, and no significant improvement was observed after 1000 scans. The 600-scan protocol was considered optimal, achieving the desired precision while saving 42% of the time compared to 1000 scans. Fig. 5(b) shows the effects of dwell time on isotope precision, and the best precision for all isotopes was obtained at 5 ms. As dwell time increased, the precision of the light isotope (B) deteriorated due to the dominance of random fluctuations, with no significant improvement observed at 50 ms, indicating that extending the dwell time

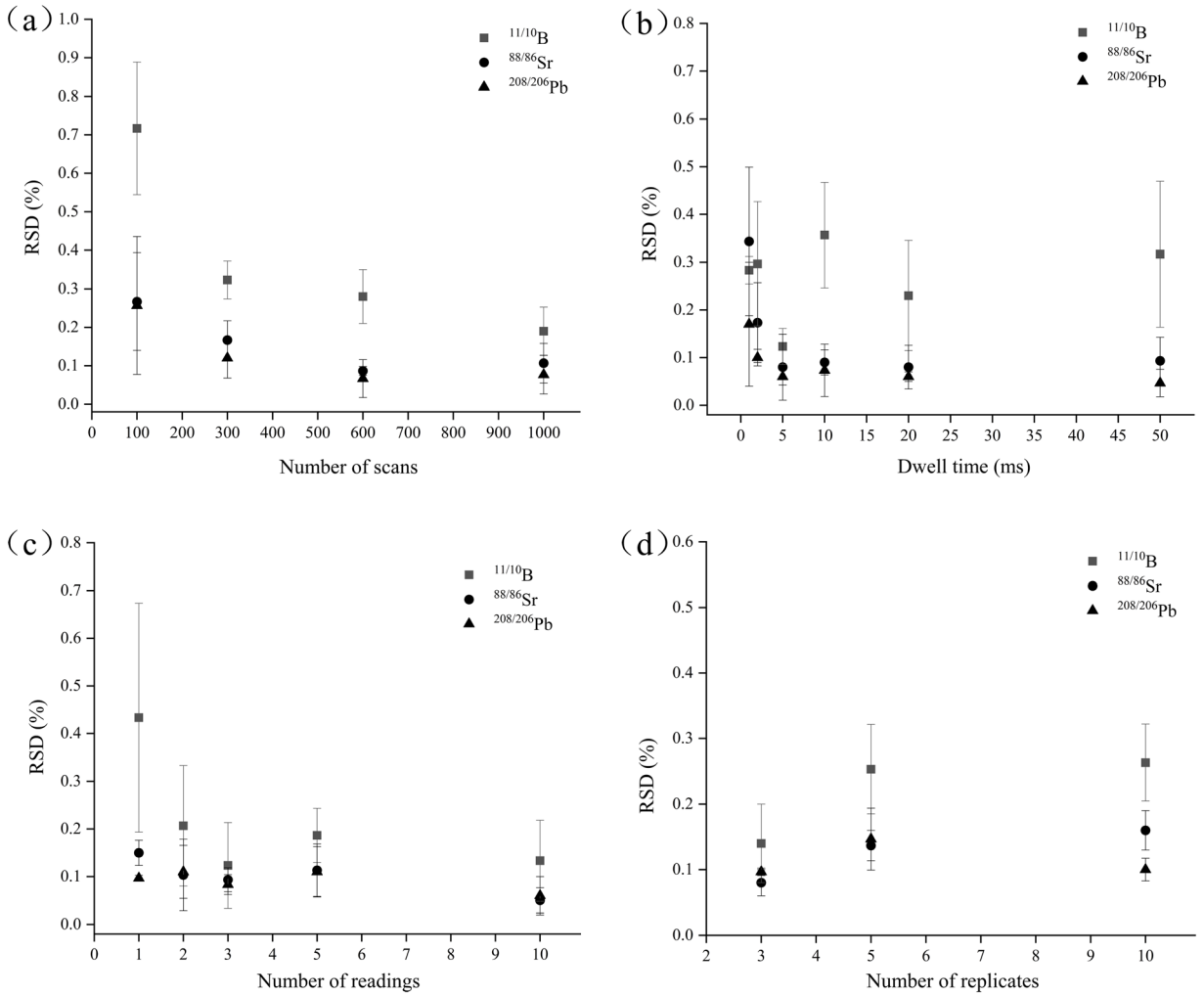

Fig. 5 Internal precision values of B, Sr, and Pb isotope ratios using different detector signal acquisition parameters: (a) number of scans, (b) dwell time, (c) number of readings, and (d) number of replicates.

failed to mitigate random noise. In contrast, Sr and Pb isotope precision remained stable below 1‰. The dwell time was set at 5 ms. Fig. 5(c) and (d) show the effects of the number of readings and replicates on isotope precision; 3 readings and 3 replicates were finally chosen as the optimal conditions, and good precision was obtained for all three isotopes.

Table 2 The analytical results for B isotopes

		δ^{11} B (mean ± 2SD, $n = 3$)		
Sample	Type	This study	Reported values (ref.)	Method
AGV-2	Andesite	−4.45 ± 0.42	−4.5 ± 1 × 10 (ref. 18)	MC-ICP-MS
			−4.18 ± 0.31 (ref. 19)	MC-ICP-MS
			−4.5 ± 0.39 (ref. 20)	MC-ICP-MS
			−4.1 ± 0.5 (2SE)[21]	MC-ICP-MS
			−3 ± 0.4 (ref. 22)	MC-ICP-MS
			−4.78 ± 0.8 (ref. 23)	MC-ICP-MS
BCR-2	Basalt	−5.86 ± 0.32	−5.93 ± 1.06 (ref. 18)	MC-ICP-MS
			−4.43 ± 0.54 (2SE)[21]	MC-ICP-MS
			−5.9 ± 0.2 (ref. 22)	MC-ICP-MS
			−5.7 ± 0.70 (ref. 32)	MC-ICP-MS
BHVO-2	Basalt	−2.71 ± 1.20	−1.61 ± 1.24 (ref. 18)	MC-ICP-MS
			−0.53 ± 0.5 (2SE)[21]	MC-ICP-MS
			−0.7 ± 0.1 (ref. 22)	MC-ICP-MS
			−2.38 ± 0.94 (ref. 32)	MC-ICP-MS

Table 3 The analytical results for Sr isotopes

		$\delta^{88/86}$ Sr (mean ± 2SD, $n = 3$)		
Sample	Type	This study	Reported values (ref.)	Method
AGV-2	Andesite	0.29 ± 0.32	0.253 ± 0.019 (ref. 33)	TIMS
			0.27 ± 0.038 (ref. 24)	MC-ICP-MS
BCR-2	Basalt	0.26 ± 0.34	0.28 ± 0.10 (ref. 36)	TIMS
			0.284 ± 0.075 (ref. 24)	MC-ICP-MS
			0.24 ± 0.09 (ref. 34)	MC-ICP-MS
			0.22 ± 0.07 (ref. 35)	MC-ICP-MS
BHVO-2	Basalt	0.27 ± 0.16	0.306 ± 0.026 (ref. 41)	TIMS
			0.248 ± 0.014 (ref. 24)	MC-ICP-MS
			0.24 ± 0.24 (ref. 34)	MC-ICP-MS

Table 4 The analytical results for Pb isotopes

		$^{208}Pb/^{206}Pb$ (mean ± 2SD, $n = 3$)		
Sample	Type	This study	Reported values (ref.)	Method
AGV-2	Andesite	2.04640 ± 0.00212	2.0417 ± 0.0004 (ref. 26)	MC-ICP-MS
			2.043 ± 0.0009 (ref. 29)	MC-ICP-MS
			2.04349 ± 0.00074 (ref. 30)	MC-ICP-MS
			2.0433 ± 0.00108 (ref. 31)	MC-ICP-MS
			2.049 ± 0.00410 (2SE)[25]	LA-ICP-MS
			2.0417 ± 0.0038 (ref. 27)	ICP-MS
			2.0415 ± 0.0026 (ref. 28)	ICP-MS
BCR-2	Basalt	2.06609 ± 0.00132	2.0646 ± 0.0008 (ref. 26)	MC-ICP-MS
			2.06528 ± 0.0001 (ref. 29)	MC-ICP-MS
			2.06516 ± 0.0009 (ref. 30)	MC-ICP-MS
			2.0653 ± 0.00118 (ref. 31)	MC-ICP-MS
			2.06385 ± 0.00004 (ref. 38)	MC-ICP-MS
			2.064 ± 0.00165 (2SE)[25]	LA-ICP-MS
			2.0647 ± 0.002 (ref. 27)	ICP-MS
			2.0635 ± 0.0032 (ref. 28)	ICP-MS
			2.067 ± 0.004 (ref. 37)	ICP-MS
			2.066 ± 0.008 (2SE)[39]	ICP-MS
			2.0658 ± 0.0065 (ref. 40)	ICP-MS
BHVO-2	Basalt	2.04952 ± 0.00308	2.0492 ± 0.001 (ref. 26)	MC-ICP-MS
			2.04949 ± 0.00033 (ref. 29)	MC-ICP-MS
			2.04921 ± 0.00007 (ref. 38)	MC-ICP-MS
			2.0516 ± 0.0038 (ref. 42)	MC-ICP-MS
			2.051 ± 0.00410 (2SE)[25]	LA-ICP-MS
			2.0507 ± 0.0032 (ref. 27)	ICP-MS
GBW07109 (GSR-7)	Syenite	2.17211 ± 0.00240	2.17237 ± 0.00004 (ref. 43)	MC-ICP-MS
GBW07364 (GSD-21)	Sediment	2.09333 ± 0.00186	2.09358 ± 0.00158 (ref. 44)	MC-ICP-MS
GBW07366 (GSD-23)	Sediment	2.10290 ± 0.00224	2.10262 ± 0.00157 (ref. 44)	MC-ICP-MS
GBW07428 (GSS-14)	Soil	2.10776 ± 0.00128	2.10713 ± 0.00003 (ref. 44)	MC-ICP-MS

3.3 Isotope analysis using geological reference materials

To verify the accuracy and precision of the established ICP-QMS isotope analysis method, we determined the B, Sr, and Pb isotopes in different geological samples, as their matrix effects are more severe than those in other types of samples. Tables 2–4 compare the measured results for B, Sr, and Pb isotopes in different geological reference materials with the reported values from the literature. As can be seen from the tables, the accuracy of the measured values of isotopes (B, Sr, and Pb) in different mass number ranges agreed with the reported values. The precision values (2SD) for B, Sr, and Pb were better than 1.20‰, 0.34‰, and 0.00308, respectively.

4. Conclusions

Optimization of the ion beam trajectory can significantly improve the accuracy of isotope analysis using ICP-QMS. The instrument voltage parameters of cell entrance/exit voltage (CEV), cell rod offset (CRO), and quadrupole rod offset (QRO) were optimized to reduce mass discrimination, and the mass deviations in B, Sr, and Pb isotope measurements were significantly reduced to −0.25%, −0.13%, and −0.34%, respectively. The detector's signal acquisition parameters were optimized to improve the precision of isotope ratio analysis. The measured B, Sr, and Pb isotope ratios of geological reference materials agreed with the reported values. This approach enables the direct analysis of diverse geological samples (rock, sediment, and soil samples) without chemical separation and purification, enabling the rapid analysis of a large number of samples. This method significantly expands the utility of ICP-QMS for precise isotope ratio determination, offering potential for geochemical fingerprinting, environmental source tracing, and other applications requiring rapidly obtained, high-precision isotopic data.

Author contributions

Xing Li: conceptualization, data curation, formal analysis, investigation, methodology, writing – original draft, writing – review and editing. Haitao Li: formal analysis, validation. Dingwen Zhang: data curation, validation. Xin Yang: methodology, formal analysis. Yu Cui: data curation, formal analysis. Wei Guo: formal analysis, supervision, writing – review and editing. Lanlan Jin: formal analysis, supervision, writing – review and editing. Shenghong Hu: conceptualization, formal analysis, funding acquisition, project administration, resources, supervision, writing –review and editing.

Conflicts of interest

There are no conflicts to declare.

Data availability

The data supporting this article are available from Mendeley Data at https://data.mendeley.com/datasets/79dpw5ddx2/2 (DOI: https://doi.org/10.17632/79dpw5ddx2.2).

Supplementary information (SI) is available. See DOI: https://doi.org/10.1039/d6ay00371k.

Acknowledgements

This work was supported by the National Natural Science Foundation of China (42473041) and the National Key R&D Program of China (No. 2021YFC2903003).

References

1 R. Santos, M. J. Canto Machado, I. Ruiz, K. Sato and M. T. S. D. Vasconcelos, *J. Anal. At. Spectrom.*, 2007, **22**, 783.
2 M. Dronov and J. Schram, *J. Anal. At. Spectrom.*, 2013, **28**, 1796–1803.
3 S. F. Boulyga, U. Klötzli, G. Stingeder and T. Prohaska, *Anal. Chem.*, 2007, **79**, 7753–7760.
4 S. Misra and P. N. Froelich, *J. Anal. At. Spectrom.*, 2009, **24**, 1524–1533.
5 X.-M. Liu and W. Li, *J. Anal. At. Spectrom.*, 2019, **34**, 1708–1717.
6 T. Ulrich, B. S. Kamber, J. D. Woodhead and L. A. Spencer, *Geostand. Geoanal. Res.*, 2010, **34**, 161–174.
7 E. Marguí, M. Iglesias, I. Queralt and M. Hidalgo, *Sci. Total Environ.*, 2006, **367**, 988–998.
8 M. R. Salazar, O. M. Bermea, E. H. Álvarez, M. E. García-Arreola and M. O. Arzate, *Geofis. Int.*, 2010, **49**, 113–117.
9 A. Usman, E. L. Ander, E. H. Bailey, S. Nelms, V. Pashley, S. D. Young and S. R. Chenery, *J. Anal. At. Spectrom.*, 2018, **33**, 2184–2194.
10 M. L. D. P. Godoy, J. M. Godoy, L. A. Roldão and L. Tauhata, *J. Environ. Radioact.*, 2009, **100**, 613–625.
11 J. Zheng and M. Yamada, *Talanta*, 2006, **68**, 932–939.
12 M. Mathuthu and N. Khumalo, *J. Radioanal. Nucl. Chem.*, 2018, **315**, 1–12.
13 Z. Wu, W. Guo, L. Jin and S. Hu, *Microchem. J.*, 2018, **142**, 251–257.
14 M. Grotti, M. A. Vecchio, D. Gobbato, M. Mataloni and F. Ardini, *J. Anal. At. Spectrom.*, 2023, **38**, 1057–1064.
15 P. A. Penanes, A. R. Galán, G. Huelga-Suarez, J. Á. Rodríguez-Castrillón, M. Moldovan and J. I. G. Alonso, *J. Anal. At. Spectrom.*, 2022, **37**, 701–726.
16 K. I. Sakata, N. Yamada and N. Sugiyama, *Spectrochim. Acta, Part B*, 2001, **56**, 1249–1261.
17 N. Kivel, I. Günther-Leopold, F. Vanhaecke and D. Günther, *Spectrochim. Acta, Part B*, 2012, **76**, 126–132.
18 Y.-H. Liu, K.-F. Huang and D.-C. Lee, *J. Anal. At. Spectrom.*, 2018, **33**, 846–855.
19 X. Li, H.-Y. Li, J. G. Ryan, G.-J. Wei, L. Zhang, N.-B. Li, X.-L. Huang and Y.-G. Xu, *Chem. Geol.*, 2019, **505**, 76–85.
20 S. Wu, Y. Yang, K. P. Jochum, R. L. Romer, J. Glodny, I. P. Savov, S. Agostini, J. C. De Hoog, S. T. Peters and A. Kronz, *Geostand. Geoanal. Res.*, 2021, **45**, 719–745.
21 Y. Cai, E. T. Rasbury, K. M. Wooton, X. Jiang and D. Wang, *J. Anal. At. Spectrom.*, 2021, **36**, 2153–2163.
22 W. Gangjian, W. Jingxian, L. Ying, K. Ting, R. Zhongyuan, M. Jinlong and X. Yigang, *J. Anal. At. Spectrom.*, 2013, **28**, 606–612.
23 J.-l. Pi, C.-F. You and C.-H. Chung, *J. Anal. At. Spectrom.*, 2014, **29**, 861–867.
24 H.-C. Liu, C.-F. You, K.-F. Huang and C.-H. Chung, *Talanta*, 2012, **88**, 338–344.
25 K. Jochum, B. Stoll, K. Herwig, M. Amini, W. Abouchami and A. Hofmann, *Int. J. Mass Spectrom.*, 2005, **242**, 281–289.
26 L. Huaikun and N. Yaoling, *Acta Geol. Sin.*, 2003, **77**, 44–58.
27 K. Newman and R. B. Georg, *Chem. Geol.*, 2012, **304**, 151–157.
28 V. Ettler, M. Mihaljevič and M. Komárek, *Anal. Bioanal. Chem.*, 2004, **378**, 311–317.
29 E. Todd, A. Stracke and E. E. Scherer, *Geochem., Geophys., Geosyst.*, 2015, **16**, 2276–2302.
30 B. Zhian, Y. Honglin, Z. Chunlei, L. Ye, C. Kaiyun and Z. Yulin, *J. Anal. At. Spectrom.*, 2016, **31**, 1012–1022.
31 R. G. Hatfield, A. V. Reyes, J. S. Stoner, A. E. Carlson, B. L. Beard, K. Winsor and B. Welke, *Earth Planet. Sci. Lett.*, 2016, **454**, 225–236.
32 G. Zhu, J. Ma, G. Wei and L. Zhang, *Geostand. Geoanal. Res.*, 2021, **45**, 583–598.
33 J. M. Brazier, A. D. Schmitt, E. Pelt, D. Lemarchand, S. Gangloff, T. Tacail and V. Balter, *Geostand. Geoanal. Res.*, 2020, **44**, 331–348.
34 F. Moynier, A. Agranier, D. C. Hezel and A. Bouvier, *Earth Planet. Sci. Lett.*, 2010, **300**, 359–366.
35 S. J. Romaniello, M. P. Field, H. B. Smith, G. W. Gordon, M. H. Kim and A. D. Anbar, *J. Anal. At. Spectrom.*, 2015, **30**, 1906–1912.
36 E. Stevenson, S. Aciego, P. Chutcharavan, I. Parkinson, K. Burton, M. Blakowski and C. Arendt, *Chem. Geol.*, 2016, **429**, 33–43.
37 M. Colombo, K. A. Brown, J. De Vera, B. A. Bergquist and K. J. Orians, *Chem. Geol.*, 2019, **525**, 479–491.
38 K. D. Collerson, B. S. Kamber and R. Schoenberg, *Chem. Geol.*, 2002, **188**, 65–83.
39 R. Tyszka, A. Pietranik, J. Kierczak, V. Ettler, M. Mihaljevič and J. Weber, *Appl. Geochem.*, 2012, **27**, 1089–1100.
40 L. S. Sherman, J. D. Blum, J. T. Dvonch, L. E. Gratz and M. S. Landis, *Sci. Total Environ.*, 2015, **502**, 362–374.
41 B. Charlier, F. Tissot, N. Dauphas and C. Wilson, *Geochim. Cosmochim. Acta*, 2019, **265**, 413–430.
42 C. Pin, A. Gannoun and A. Dupont, *J. Anal. At. Spectrom.*, 2014, **29**, 1858–1870.
43 Y. H. Yang, M. Yang, K. P. Jochum, S. T. Wu, H. Zhao, L. W. Xie, C. Huang, X. C. Zhan, J. H. Yang and F. Y. Wu, *Geostand. Geoanal. Res.*, 2020, **44**, 567–579.
44 G. Wu, J.-M. Zhu, D. Tan, G. Han, L. Zhang and K. Ren, *Acta Geochim.*, 2017, **36**, 421–425.